Check for updates

JGR Space Physics

RESEARCH ARTICLE
10.1029/2024JA033691

Special Collection:
Space Weather Events of 2024 May 9-15

Key Points:

- Following a ~120 nT flip of interplanetary magnetic field B_Y, the northward ground magnetic component abruptly changed as much as 4300 nT in the midday auroral zone
- It took ~10 min for the midday auroral electrojet to change its direction after the B_Y flip was observed in the dayside magnetosheath
- The prolonged delay may be attributed to the reduction of the reconnection rate at the magnetopause due to solar wind density enhancement

Correspondence to:
S. Ohtani,
ohtani@jhuapl.edu

Citation:
Ohtani, S., Zou, Y., Merkin, V. G., Wiltberger, M., Pham, K. H., Raptis, S., et al. (2025). Ground magnetic response to an extraordinary IMF B_Y flip during the May 2024 storm: Travel time from the magnetosheath to dayside high latitudes. *Journal of Geophysical Research: Space Physics*, *130*, e2024JA033691. https://doi.org/10.1029/2024JA033691

Received 3 JAN 2025
Accepted 20 APR 2025

Ground Magnetic Response to an Extraordinary IMF B_Y Flip During the May 2024 Storm: Travel Time From the Magnetosheath to Dayside High Latitudes

S. Ohtani[1], Y. Zou[1], V. G. Merkin[1], M. Wiltberger[2], K. H. Pham[2], S. Raptis[1], M. Friel[1], and J. W. Gjerloev[1]

[1]Johns Hopkins University Applied Physics Laboratory, Laurel, MD, USA, [2]National Center for Atmospheric Research, High Altitude Observatory, Boulder, CO, USA

Abstract In the present study we investigate the response of the dayside ground magnetic field to the sequence of interplanetary magnetic field (IMF) B_Y changes during the May 2024 geomagnetic storm. We pay particular attention to its extraordinarily large (>120 nT) and abrupt flip, and use GOES-18 (G18) magnetic field measurements in the dayside magnetosheath as a time reference. In the dayside auroral zone, the northward magnetic component changed by as much as 4,300 nT from negative to positive indicating that the direction of the auroral electrojet changed from westward to eastward. The overall sequence was consistent with the conventional understanding of the IMF B_Y driving of zonal ionospheric flows and Hall currents, which is also confirmed by a global simulation conducted for this storm. Surprisingly, however, the time delay from G18 to the ground increased significantly in time. The delay was 2–3 min for a sharp B_Y reduction ~30 min prior to the B_Y flip, but it became as long as 10 min for the zero-crossing of the B_Y flip. It is suggested that the prolonged time delay reflected the travel time from G18 to the reconnection site, which sensitively depends on the final velocity at the magnetopause, that is, the inflow velocity of the magnetic reconnection. Around the B_Y flip, the solar wind number density transiently exceeded 100 cm^{-3}, and should have increased further through the bow shock crossing. It is suggested that this unusually dense plasma reduced the reconnection rate, and therefore, the solar wind-magnetosphere energy coupling due to the extraordinary IMF.

Plain Language Summary The present study examines how the ionospheric current system responded to changes in the interplanetary magnetic field (IMF) during a major geomagnetic storm in May 2024. Following an abrupt change in the IMF direction, the ionospheric current changed its direction from westward to eastward in the dayside auroral zone. This ionospheric response can be well explained by magnetic reconnection, that is, merging between interplanetary and terrestrial magnetic field lines. In this event, however, the ionospheric current responded ~10 min after the IMF change was observed by a geosynchronous satellite, although the time delay is usually only a few minutes. This prolonged time delay suggests that the reconnection occurred very slowly, possibly due to an extremely dense plasma that was observed in the solar wind along with the IMF change. Therefore, this event may serve as a rare demonstration of how solar wind density impacts energy transport to the geospace system.

1. Introduction

During a geomagnetic storm that took place on 10–13 May 2024, known as the Mother's Day storm or the Gannon storm, the Dst index reached −412 nT at its peak making this storm the most intense storm in more than two decades (as measured by the peak Dst; e.g., Cliver and Svalgaard, 2004; Love, 2021). The external driving of this superstorm consisted of a series of distinct periods of enhanced southward interplanetary magnetic field (IMF) B_Z, and the IMF B_Y component also revealed large sudden changes. The focus of this study is the response of ground magnetic fields to an extraordinarily large and abrupt change of IMF B_Y, which took place near the peak of this superstorm.

Whereas the IMF B_Z component is crucial for the energy coupling between the solar wind and magnetosphere, the IMF B_Y component is the primary cause of dawn-dusk asymmetries of the magnetosphere-ionosphere (M-I) system (e.g., Cowley et al., 1992), with its effects being most profound in midday high latitudes. Early studies found that the northward ground magnetic component increases in the cusp region in Northern Hemisphere when IMF B_Y is positive, and decreases when it is negative (Friis-Christensen and Wilhjelm, 1975). In the same area, the

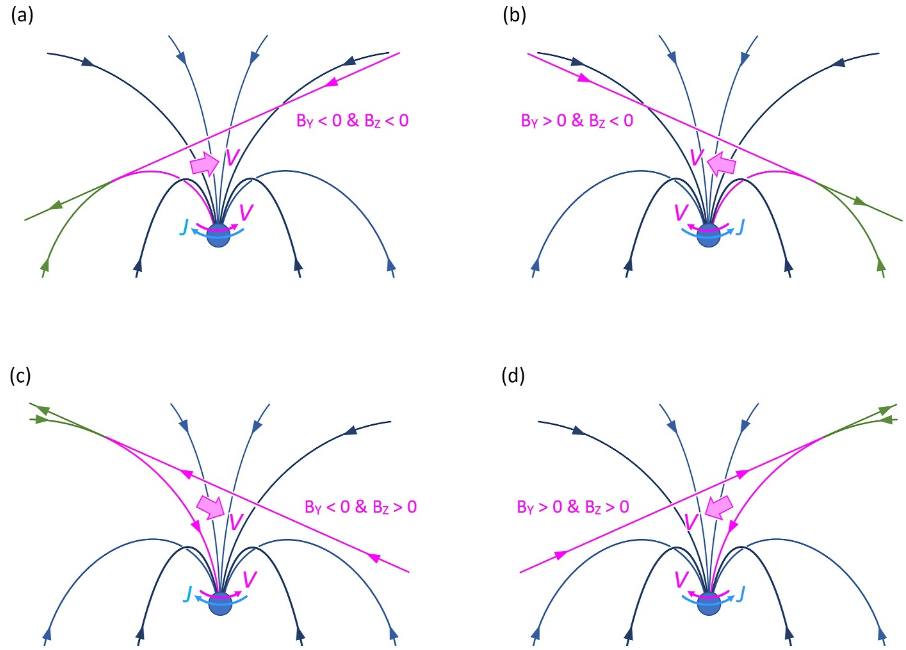

Figure 1. Schematic illustration of the reconnection-driven convection and Hall current in the midday sector for (a) $B_Y < 0$ and $B_Z < 0$, (b) $B_Y > 0$ and $B_Z < 0$, (c) $B_Y < 0$ and $B_Z > 0$, and (d) $B_Y < 0$ and $B_Z > 0$. In each panel, the magenta field line represents a newly reconnected open field line, the subsequent motion of which drives a zonal ionospheric flow (magenta arrow) and a Hall current (blue arrow), that is, AEJ, in the dayside high-latitude region. The green field line illustrates a newly reconnected interplanetary field line.

zonal ionospheric convection tends to be directed westward for positive IMF B_Y, and eastward for negative IMF B_Y (Heelis, 1984), which is consistent with the idea that the aforementioned ground magnetic disturbance can be attributed to zonal Hall currents, that is, auroral electrojets (AEJs). This zonal current is apparently accompanied by a pair of field-aligned currents (FACs), the polarities of which change depending on the sign of IMF B_Y (Iijima et al., 1978; Wilhjelm et al., 1978). These effects of IMF B_Y are not confined to the midday sector, and if IMF B_Y remains steady, global patterns are established (Burch et al., 1985; Edwards et al., 2020; Heppner and Maynard, 1987; Weimer, 2005). For positive IMF B_Y, the M-I system in Northern Hemisphere is characterized by the clockwise (westward) swirling of convection flows over the polar region, and the swirling of the opposite sense for the AEJs. For negative IMF B_Y, the sense of the swirling is reversed, that is, counter-clockwise (eastward) for convection flows and clockwise (westward) for the AEJs.

The IMF B_Y dependence of the dayside M-I coupling can be explained by the reconnection between interplanetary and terrestrial magnetic field lines (e.g., Cowley et al., 1992) as schematically summarized in Figure 1. When IMF B_Y is negative and positive with southward IMF B_Z, the dayside magnetic reconnection site has its magnetic footprint at prenoon and postnoon, respectively, in Northern Hemisphere (Figures 1a and 1b). The associated magnetic stress pulls the reconnected field lines eastward for negative IMF B_Y, and westward for positive IMF B_Y, driving zonal ionospheric flows. Accordingly, the associated Hall current (i.e., AEJ) is directed westward for negative B_Y causing southward ground magnetic disturbances, and eastward for positive IMF B_Y causing northward ground magnetic disturbances. The direction of the magnetic tension, and thus the direction of the AEJ, is determined by the sign of IMF B_Y, and remains unchanged regardless of the sign of IMF B_Z; compare Figure 1a with Figure 1c, and Figure 1b with Figure 1d. Though, when IMF B_Z is positive, the reconnection site moves to behind the dayside cusp. These processes well explain the aforementioned observational features, strongly suggesting that magnetic reconnection is essential for the IMF B_Y dependence of the M-I coupling.

This conventional understanding of the IMF B_Y dependence of the M-I system should also apply to the IMF B_Y flip of the May 2024 storm, the focus of the present study. Nevertheless, as will be shown in this paper, the present event provides new insight into the IMF B_Y driving of the M-I current system from two important perspectives. First, because of its large magnitude and abruptness of this B_Y flip, along with its spatial scale as observed by multiple satellites, this B_Y flip serves as an unambiguous time reference. The associated ground magnetic disturbances can also be identified unambiguously. Therefore, we can confidently discuss underlying physics of the time delay from the solar wind to the dayside ionosphere. Second, the observed ground magnetic disturbances were at least comparable in (peak-to-peak) magnitude with those of extreme events on the nightside. Therefore, the present event helps recognize that extraordinary IMF B_Y, as a driver of dayside AEJs, can be a cause of potentially hazardous geomagnetic disturbances even though it is seldom discussed from the perspective of space weather.

The rest of this study is organized as follows. In Section 2 we briefly examine the solar wind and IMF sequences of this storm with emphasis on the sequence of the B_Y component as observed by the GOES-18 (G18) geosynchronous satellite in the dayside magnetosheath, then examine in detail how the AEJs responded focusing on the time delay from G18 to the ground. In Section 3, we briefly compare the observation with the result of a global simulation, which was conducted for this storm in a separate study (Pham et al., 2024). In Section 4, we will discuss the time delay from G18 to the ground. We summarize this study in Section 5.

2. Observation

2.1. Solar Wind and IMF Signatures

In this subsection, we briefly examine the solar wind and IMF sequences of the May 2024 storm. Figure 2 shows SuperMAG geomagnetic indices, SMR and SMU/SML, and OMNI IMF and solar wind parameters for the 12-hr interval from 1630 UT on 10 May to 0430 UT on 11 May 2024. SMR is equivalent to the *Sym-H* index but based on data from geomagnetic stations in a wider range of geomagnetic latitude (MLat), from −50° to +50° in MLat (Newell & Gjerloev, 2012). Similarly, SMU and SML are equivalent to the AU and AL indices, respectively, but based on data from geomagnetic stations at +40° to +80° in MLat (Newell & Gjerloev, 2011); SMU and SML are the measurements of the eastward and westward AEJs, respectively. For this interval, both the solar wind and IMF parameters of the OMNI database were measured by the Wind satellite around the L1 point, and propagated to the subsolar bow shock. Frequent data gaps reflect undetermined propagation time.

SMR suddenly jumped by more than 100 nT at 1705 UT on 10 May 2024 (Figure 2a), which marks the storm sudden commencement (SSC) of this storm. SMR reached a minimum at −413 nT at 2236 UT, followed by another minimum in less than 4 hr, then made a more persistent recovery. IMF B_Z intermittently became strongly negative occasionally reaching ∼−40 nT (Figure 2e). Whereas the solar wind speed stayed around 700 km after the SSC (Figure 2g), fluctuations are noticeable for the solar wind density (Figure 2h), and therefore, for the dynamic pressure (Figure 2f).

Around the time of the first SMR minimum, IMF B_Y sharply changed from strongly negative (∼−60 nT) to strongly positive (∼+70 nT) as marked by the dashed line (Figure 2d), which was the most noticeable IMF feature during the entire interval of this storm. Simultaneously with this IMF B_Y flip, IMF B_Z also changed from negative to positive, but this positive IMF B_Z was transient (Figure 2e). The associated change of IMF B_X was far less significant (Figure 2c). Right after the IMF B_Y flip, SML made a large negative (∼−2,400 nT) spike, which was immediately followed by a large positive spike (∼+2,300 nT) of SMU (Figure 2b). In the next subsection we will examine the associated change of the AEJ distribution in more detail with a focus on its timing.

Now we examine the spatial extent and timing of this IMF B_Y flip. In addition to the Wind satellite, several satellites were located in either solar wind or magnetosheath as shown in Figure 3a. The two probes of the Acceleration, Reconnection, Turbulence and Electrodynamics of the Moon's Interaction mission with the Sun (ARTEMIS), ThB and ThC, were located in the upstream region, at $X_{\text{gse}} = \sim+47\ R_E$ and $Y_{\text{gse}} = \sim+37\ R_E$. The Magnetospheric Multiscale (Magnetospheric Multiscale (MMS)) Probes, which is represented by Probe 1 (MMS1) in this study because of their close proximity, were located much closer to Earth ($X_{\text{gse}} = \sim+11\ R_E$) and on the opposite (i.e., negative Y_{gse}) side of the Sun–Earth line, at $Y_{\text{gse}} = \sim-20\ R_E$. In addition, the GOES-18 geosynchronous satellite (G18) was in the postnoon magnetosheath. All these satellites were close to the ecliptic plane (Figure 3b).

Figures 4a–4c show three magnetic components observed by those spacecraft in different colors along with the OMNI data (black dotted) for the 80 min interval of 2150–2310 UT. The sequences of each component observed by different satellites are similar to each other, as well as to the OMNI data, but with time delays expected from the propagation of the solar wind. Therefore, considering the distribution of the satellites (Figure 3), we conclude

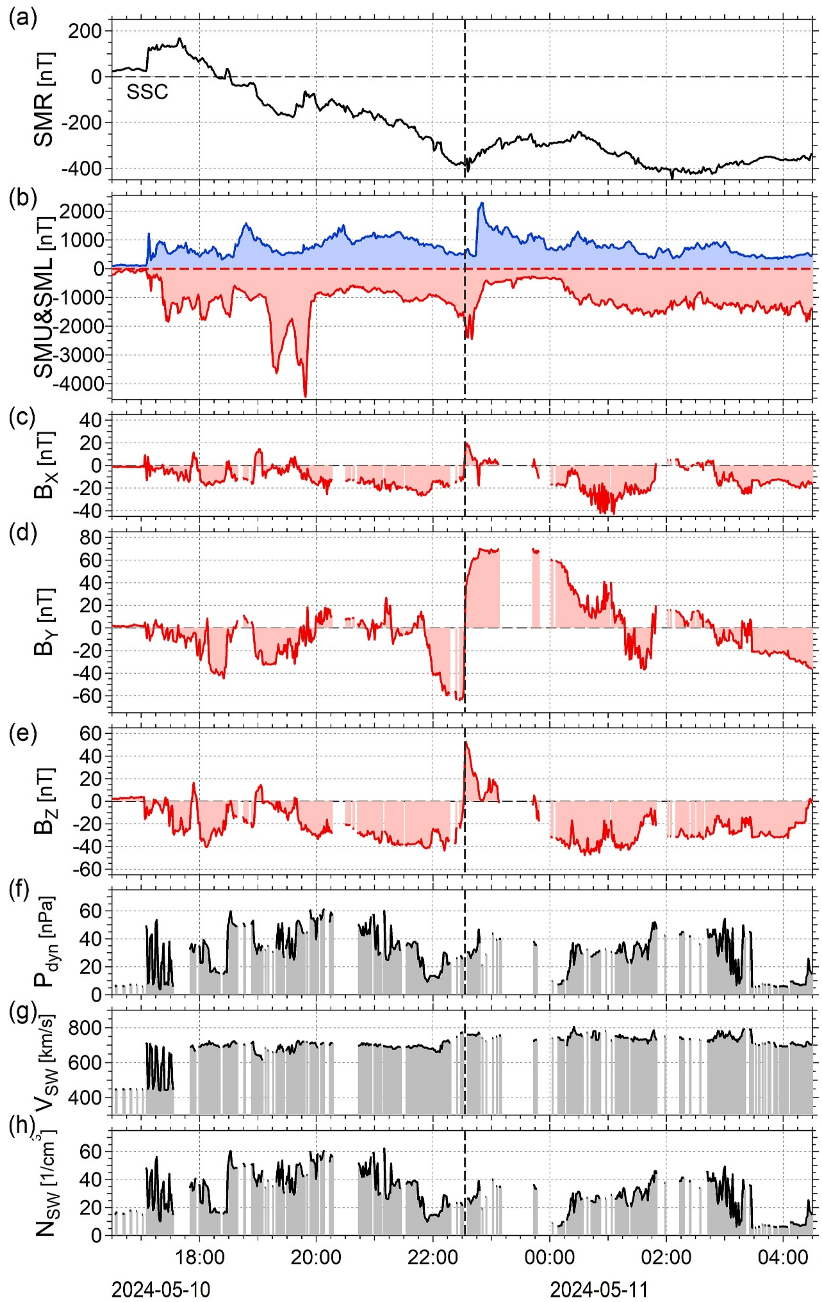

Figure 2. (a) SMR, and (b) SMU (blue) and SML (red) indices, and IMF (c) B_X, (d) B_Y, (e) B_Z, solar wind (f) dynamic pressure P_{dyn}, (g) speed V_{SW}, and (h) density N_{SW} during the 12-hr interval from 1630 UT on 10 May to 0430 UT on 11 May 2024. The IMF and solar wind parameters were obtained from the OMNI database.

that the IMF structures, including the flip of IMF B_Y, extended extensively in the $Y-Z$ plane, and it certainly interacted with the magnetosphere.

B_Z was negative at G18 before the B_Y flip, indicating that the satellite was outside of the magnetosphere. Note also that for G18, each component is multiplied by 0.25. That is, the actual G18 measurements were four times larger in magnitude. Presumably, G18 was in the magnetosheath, and observed the magnetic field compressed through the bow shock. G18 probably stayed in the magnetosheath for a while after the B_Y flip (as suggested by the similarity of the variations of each component to those observed by other satellites), then reentered the magnetosphere around 2252 UT, when each component changed abruptly. Considering also that G18 was close to the

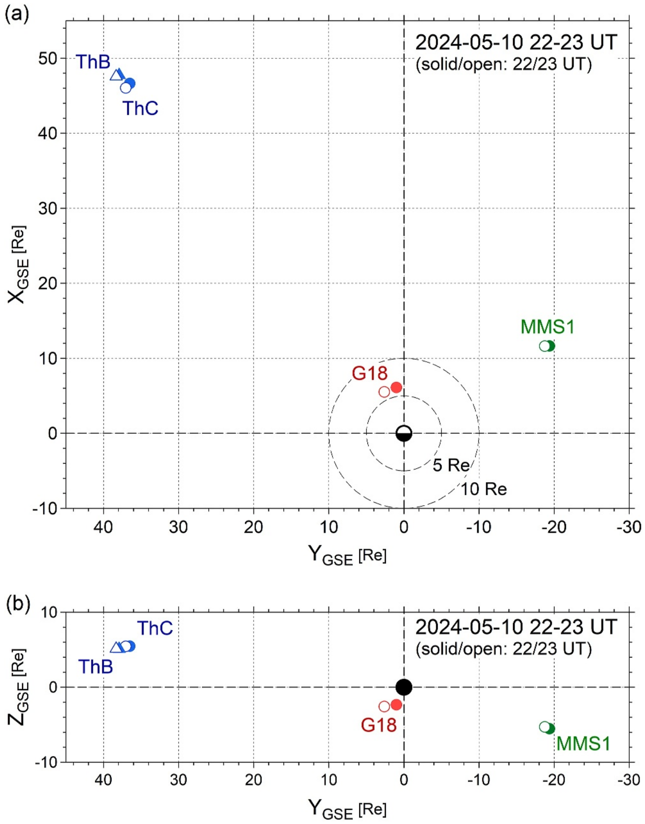

Figure 3. Locations of ThB (blue triangle), ThC (blue circle), MMS1 (green), and G18 (red) in the GSE (a) X−Y and (b) Y−Z planes at 22 (solid) and 23 (open) UT on 10 May 2024.

Sun–Earth line (Figure 3; LT = UT–9.1), we will use the G18 magnetic measurement as a reference in the rest of this study.

Figures 4d and 4e show the solar wind number density (N_{SW}) and velocity (Vsw) measured by ThC (blue) and MMS1 (green), respectively; G18 does not carry a plasma instrument. At ThC and MMS1, N_{SW} had an isolated peak centered at the B_Y flip. In contrast, Vsw stayed in a limited range since it increased by ∼100 km/s around 2200 UT. Accordingly, the variations of N_{SW} at ThC and MMS1 can be considered to be parallel to those of dynamic pressure. Figure 4d also plots the ground N component at dayside midlatitude stations, Fresno (FRN; red solid), Tucson (TUC; red dashed), and Bay St Louis (BSL; red dotted); see Table 1 for the locations of these ground stations. The N component is the disturbance part of the horizontal magnetic component pointing local magnetic north as calculated by the SuperMAG routine procedure (Gjerloev, 2012). The N component peaked at 2235 UT, at the same time as the zero-crossing of the G18 B_Y flip; the timing may be more easily confirmed later in Figure 5a. This result strongly suggests that the effect of the dynamic pressure enhancement propagated with a minimal delay (∼1 min) from G18 to the ground, which is reasonable since the propagation speed of the compression wave (fast magnetosonic wave) easily exceeds 1,000 km/s (10 R_E/min) in the magnetosphere.

2.2. Ground Magnetic Disturbances

The sudden transition of polar magnetic disturbances reflected in the SML and SMU indices, as shown in Figure 2b, is consistent with the general understanding of the dayside AEJ response to the negative-to-positive IMF B_Y flip (Section 1). In this subsection, we examine how this transition of the AEJ took place in space.

Figure 5 shows, from the top, the G18 B_Y and B_Z components along with the dayside midlatitude N component (Figure 5a), SMU/SML (Figure 5b), and the LT sub-indices of SMU and SML, SMUhh's (Figure 5c) and SMLhh's (Figure 5d). SMUhh's and SMLhh's are defined in the same way as SMU and SML, the upper and lower envelops of the ground N component, respectively, but based on data within 3 hr in MLT centered at MLT = hh.

Preceding the extraordinary B_Y flip, G18 observed a sharp reduction of B_Y starting at 2201–2202 UT (Figure 5a). Around the same time, SML started to decrease gradually (Figure 5b), which reflected the enhancement of SMLhh's from midnight, through dawn, to noon in MLT (Figure 5d); the gap at MLT = 07 was probably due to the lack of high-latitude ground stations in the corresponding sector (Figure 6). In the dusk-to-midnight sector, in contrast, the decrease of SMLhh's was insignificant. Therefore, the associated intensification of the westward AEJ can be attributed to the enhancement of global convection rather than nightside substorm activity.

Interestingly, after the B_Y flip at G18, the westward AEJ intensified further in the prenoon sector as indicated by the enhancement of dayside SMLhh's (Figure 5d). This prenoon westward AEJ decayed suddenly in ∼10 min, and it was immediately replaced by an intense eastward AEJ (Figure 5c). In the early dawn sector, in contrast, the westward AEJ remained intense for a while even after the direction of the midday AEJ turned eastward, then decayed slowly. In the noon-to-dusk sector, the intense eastward AEJ gradually expanded in MLT. Thus, the abrupt swing from SML to SMU reflected the flip of the AEJ direction from westward to eastward in the midday sector, and the transition was more gradual away from the midday sector.

Now we address how the polar distribution of AEJs changed as the G18 B_Y component changed. Figure 6 shows the SuperMAG polar map of ground magnetic disturbances every 10 min from 2210 to 2300 UT; the six dots labeled as a–f in Figure 5b mark the times corresponding to these six polar maps. The horizonal magnetic disturbance vectors are rotated clockwise by 90°, and accordingly, each map may be considered as a polar distribution of equivalent currents (but in units of nT), and is also indicative of ionospheric convection if the Hall current is the predominant cause of high-latitude ground magnetic disturbances as usually expected.

10.1029/2024JA033691

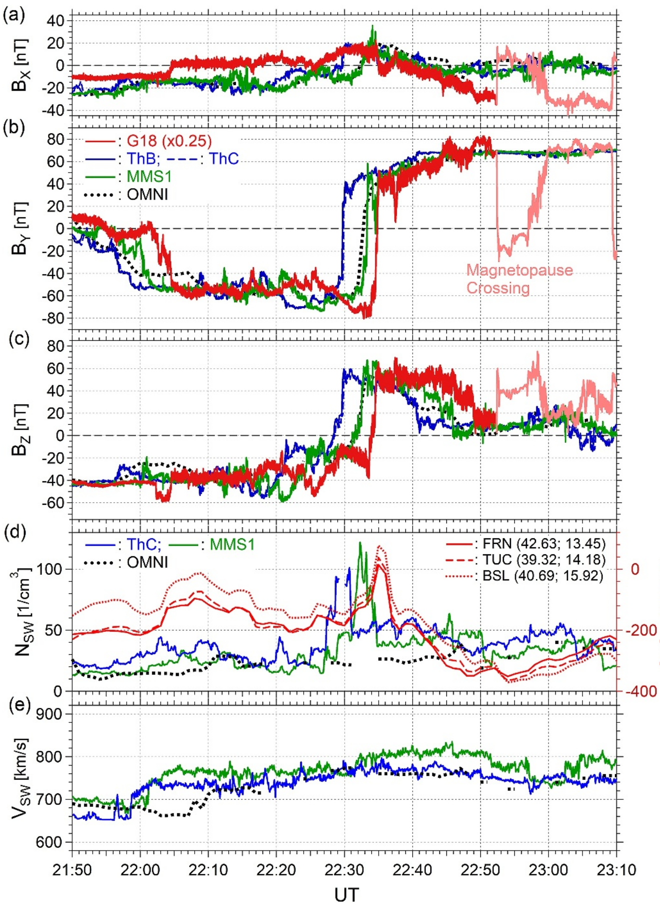

Figure 4. (a) B_X, (b) B_Y, and (c) B_Z components in GSM, (d) N_{SW}, and (e) V_{SW}, observed by G18 (red), ThB (blue solid), ThC (blue dashed), MMS1 (green) along with the OMNI data (black dotted) for the interval from 2150 to 2310 UT on 10 May 2024. The G18 magnetic field measurements are multiplied by 0.25. No plasma density and flow speed data are available for G18. In Panel d, N-component magnetic disturbances observed at Fresno (FRN; red solid), Tucson (TUC; red dashed), and Bay St Louis (BSL; red dotted) in dayside midlatitudes are also plotted (scaled on the right axis).

At 2210 UT, ∼5 min after IMF B_Y decreased sharply, the dawn and dusk cells still coexisted as indicated by the clockwise and counter-clockwise swirling of magnetic disturbance vectors on the dawn and dusk sides, respectively; see the magenta dashed lines in Figure 6a. However, in the next 30 min, the dusk cell diminished (Figure 6b–6d), and in the midday sector, the vectors became predominantly westward and intensified corresponding to the SMLhh enhancement in the midday sector. Note that 5 min after the G18 B_Y flip, the vectors in dayside high latitudes not only remained westward but also enhanced (Figure 6d). However, by 2250 UT (Figure 6e), they flipped eastward corresponding to the enhancement of SMUhh's in the midday sector. In the next 10 min, the counter-clockwise swirling of magnetic disturbance vectors developed further but mostly on the dayside; see the magenta dashed lines in Figure 6f. Thus, the polar distribution of magnetic disturbances evolved as expected for the negative-to-positive B_Y flip, but it reconfirms that the AEJ system responded to the G18 B_Y flip with a noticeable time delay.

2.3. Time Delay From G18 to Midday High Latitudes

Next, we examine the sequence of magnetic disturbances at individual stations. Figures 7a–7f (six panels in the left column) show the three magnetic components, N (northward; red), E (eastward; green), and Z (vertically downward; blue) observed at six stations in the midday sector, as marked by the orange dots in Figure 7m, in the descending order of MLat; see Table 1 as well as the inserts for their coordinates.

N (red) started to decrease around 2205 UT at each station indicating an intensification of the westward AEJ, which can be attributed to the sudden reduction of the G18 B_Y component at 2202 UT. At Deadhorse (DED), N initially remained flat, but E started to increase earlier. Similar E enhancements were observed at other stations around the same time as the N reduction. Since the stations were located in the sector of convection throat as suggested by Figure 6a, those eastward magnetic disturbances may have been caused by a local Hall current flowing equatorward corresponding to poleward ionospheric convection. Additionally, at lower-latitude stations, the N reduction was preceded by a bump, which also obscured its start time. Nevertheless, we can conclude that the G18-to-ground time delay was a few minutes at most.

Most noticeably, N changed sharply from negative to positive around 2244 UT corresponding to the westward-to-eastward flip of the AEJ direction. The peak-to-peak amplitude was largest at Barrow (BRW), where N changed by more than 4300 nT, from −2,450 nT to +1,860 nT, in 11 min from 2240 to 2251 UT (Figure 7b). This N flip occurred ∼10 min after the G18 B_Y flip, creating a clear contrast to the AEJ response to the earlier B_Y reduction at 2202 UT.

We also note that the magnitude of the overall N variation was apparently not organized by MLat; it had a local minimum at Fort Yukon (FYU; Figure 7c); compare with the N component at BRW (Figure 7b) and College (CMO; Figure 7e), the next poleward and equatorward stations, respectively. The MLat dependence of the Z variation was also complex; for the N flip, for example, Z decreased at Deadhorse (DED; Figure 7a) and CMO (Figure 7e), but increased at FYU (Figure 7c). These features may suggest that the AEJ intensity had more than one peak in MLat. Ground induction may also have contributed to the complexity of the MLat distribution of the ground magnetic disturbances.

Figures 7g–7l (six panels in the right column) show magnetic disturbances observed at six stations in the postnoon-to-early dusk sector in the ascending order of MLTs; their locations are marked by the purple dots in Figure 7m. Here again, we can find that the the N component turned from negative to positive around 2245 UT. However, compared with the signatures in the midday sector (Figures 7a–7f), the transition was gradual and small in magnitude; the magnitude of the N flip was largest in the midday sector, and decreased duskward.

Table 1
Geographic and Geomagnetic Latitudes and Longitudes of the Ground Stations Used in the Present Study, and Their MLTs at 2240 UT on 10 May 2024

Code	Station	GLat	GLon	MLat	MLon	MLT (2240 UT)
BSL	Bay St Louis	30.4	270.4	40.7	−17.9	15.9
BRW	Barrow	71.3	203.4	70.6	−106.5	11.0
CMO	College	64.9	212.1	65.5	−93.8	11.8
DED	Deadhorse	70.4	211.2	70.9	−99.3	11.5
EAG	Eagle	64.8	218.8	66.6	−87.8	12.2
FCC	Fort Churchill	58.8	265.9	68.5	−25.6	16.4
FRN	Fresno	37.1	240.3	42.6	−54.9	13.5
FSP	Fort Simpson	61.8	238.8	67.5	−64.9	13.8
FYU	Fort Yukon	66.6	214.8	67.7	−92.8	11.9
GAK	Gakona	62.4	214.9	63.4	−89.9	12.1
GIM	Gillam	56.4	265.4	66.2	−26.1	16.4
IQA	Iqaluit	63.8	291.5	72.2	15.6	19.1
PKR	Poker Flat	65.1	212.6	65.8	−93.6	11.8
RAL	Rabbit Lake	58.2	256.3	67.0	−40.1	15.4
SMI	Fort Smith	60.0	248.1	67.5	−52.3	14.6
TUC	Tucson	32.2	249.3	39.3	−52	14.2

As a side note, we also point out that N made a small dip for 2234–2237 UT at each station shown in Figures 7g–7l. The corresponding dip can also be found for the six midday stations (Figures 7a–7f) although they were less clear because of concurrent larger disturbances. Apparently, these N dips were global, and their timing was coincident with the midlatitude N enhancements observed simultaneously with the G18 B_Y flip (Figures 4d and 5a). Therefore, we conclude that the observed dips can be attributed to the external compression rather than magnetic reconnection; see Araki (1994) for more details of such compression-related magnetic disturbances.

Figure 8a shows the N component measured at the six stations in the midday sector (Figures 7a–7f) in orange, and the same but at the six stations at later MLTs (Figures 7g–7l) multiplied by 1.75 in purple, and the G18 B_Y component in gray (scaled on the right axis) on top of each other. The distinction of the stations is not important for the present exercise. Although the magnitudes were different, the signatures were well correlated among the 12 stations despite the wide range of their MLT coverage (Figure 7m). That is, the midday AEJ changed almost simultaneously from prenoon to dusk. Though, the differences were more noticeable after 2250 UT; N peaked earlier in time in the midday sector (orange lines) than at later MLTs (purples lines). This is consistent with the general idea that the global ionospheric current and convection start to respond simultaneously to changes in external driving (Murr and Hughes, 2001; Ruohoniemi and Greenwald, 1998), but it takes more time farther from the midday sector to reach steady states (Ridley et al., 1998).

We take a closer look at the time delay of the dayside AEJ response for the following four changes of the G18 B_Y component, which are marked as numbers 1 to 4 in Figure 8a.

1. G18 B_Y started to decrease sharply at 2201:30 UT, and the ground N component decreased subsequently. As we addressed earlier, the G18-to-ground time delay was 2–3 min, and possibly shorter, which may be consistent with the general expectation that one might have for a propagation time from the dayside magnetosheath to the dayside high-latitude auroral zone.
2. B_Y started to decrease further at 2226:00 UT. Although a further intensification of the westward AEJ is expected, the ground N component started to recover in the entire midday sector with small, but noticeable, magnitudes. One possible interpretation is that this N recovery was actually an effect of a small (~30 nT) increase of the G18 B_Y component observed at 2219 UT, 6–7 min earlier; for the time delay for this feature, see the next feature described below.
3. B_Y started to flip at 2233:50 UT. The expected ionospheric response is a sharp decay of the preexisting westward AEJ, and therefore, a sudden recovery of the negative N disturbance on the ground. However, the N component started to decrease further at 2234 UT. Physically, it is more reasonable to associate (a) this additional N reduction with the preceding B_Y reduction at 2226 UT, which we identified as (2), and (b) the start of the B_Y flip with the start of the later flip of the ground N component. For (a), the time delay was ~8 min. For (b), the N flip started at 2240–2244 UT, but either at 2241 or 2242 UT at most stations. Therefore, the time delay was 7~8 min.
4. B_Y made a zero-crossing at 2234:45 UT, which we adopt as a time reference for the B_Y flip. As a manifestation of its effect on the dayside AEJ, we consider the zero crossing of the ground N component, which can be attributed to two processes. One is the decay of the westward AEJ driven by the preceding negative B_Y-related reconnection at prenoon. Another is the intensification of the eastward AEJ driven by the subsequent positive-B_Y related reconnection at postnoon. Since the G18 B_Z component turned northward as B_Y flipped, this latter reconnection presumably took place at the high-latitude boundary layer (i.e., tailward of the cusp). These two processes probably contributed to the zero crossing of the ground N component in different ways at different MLT's, and possibly also at different MLat's. In fact, Figure 8a shows that the timing of the zero crossing varied significantly. Referring to earlier timings of them, we conclude that the G18-to-ground time delay was 9–10 min for the zero crossing of G18 B_Y.

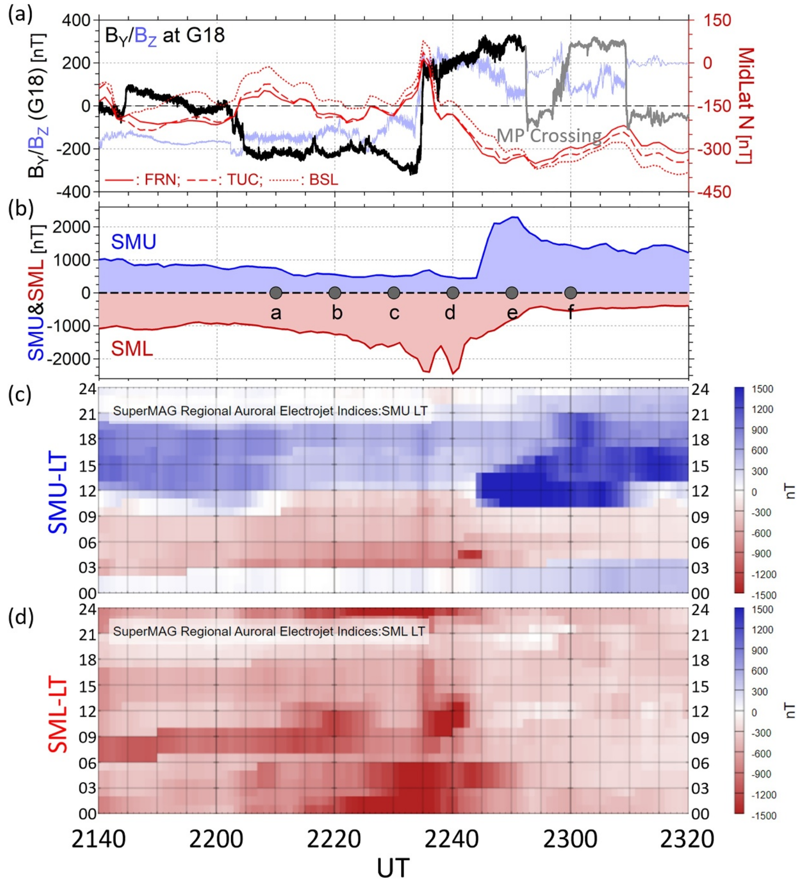

Figure 5. (a) B_Y (dark/light gray) and B_Z (light blue) at G18 (not multiplied by 0.25) along with the N-component magnetic disturbances observed at Fresno (FRN; red solid), Tucson (TUC; red dashed), and Bay St Louis (BSL; red dotted), (b) SMU and SML, (c) SMUhh's, and (d) SMLhh's for the interval of 2140–2320 UT on 10 May 2024. The six dots labeled as a–f in Panel b mark the times corresponding to the six polar maps of ground magnetic disturbances shown in Figure 6.

The G18-to-ground time delay changed in time over ~40 min. It was initially a few minutes, but it became as long as 10 min for the B_Y flip. As a demonstration, we show in Figure 8b the G18 B_Y component shifted by +570 s (9.5 min) in red, and the N sequences at all 12 stations in gray. The G18 B_Y component is also shifted vertically by +110 nT for easy comparison. For the second and third B_Y features that we discussed above, the shifted G18 B_Y plot traces the ground N component reasonably well. However, the discrepancy of the timing is obvious for the first B_Y reduction. This time-varying time delay will be the focus of discussion in Section 4.

2.4. PFISR Observations

In closing of this section, we examine the sequence of local ionospheric quantities measured by the Poker Flat Incoherent Scatter Radar (PFISR), which is located in the neighboring area of FYU and CMO (Figure 7m). Figure 9a shows the altitudinal profile of the electron density, N_e, as measured by a beam approximately vertical and aligned with the local magnetic field (beam 2 in Figure 9f), for 2150–2310 UT. Most noticeably, N_e suddenly enhanced at ~2243 UT in a wide range of altitude down to 100 km, which suggests enhanced precipitation of not only soft electrons but also energetic electrons. Therefore, the associated precipitation was possibly Alfvénic reflecting a temporal change of a certain magnetospheric process.

In general, the ionospheric conductance increases with increasing N_e. Figure 9b shows the sequence of the local Pedersen and Hall conductances, which we estimated by integrating over altitude, h, the Pedersen and Hall conductivities as expressed by the following equations

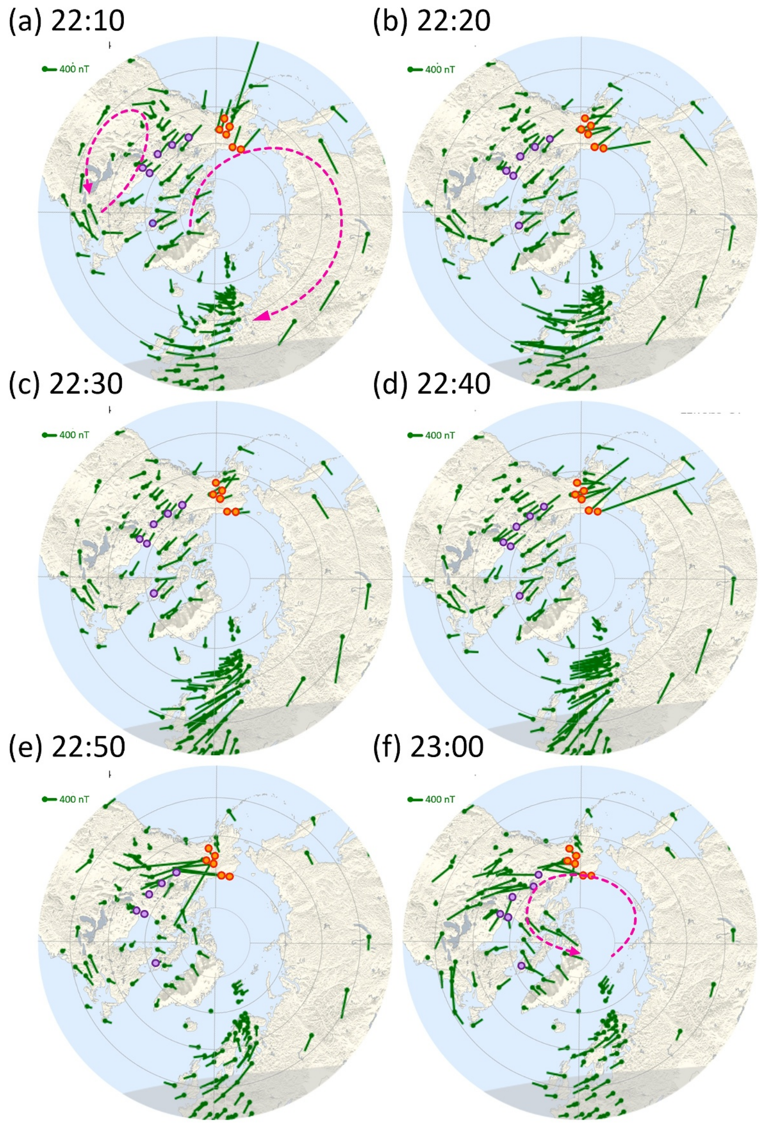

Figure 6. Polar map of horizontal ground magnetic disturbances (rotated clockwise by 90°) at (a) 2210, (b) 2220, (c) 2230, (d) 2240, (e) 2250, and (f) 2300 UT. The orange and purple dots mark stations examined in Figure 7.

$$\sigma_P(h) = \frac{eN_e(h)}{B(h)}\left[\frac{\nu_{en}\Omega_e}{{\nu_{en}}^2 + {\Omega_e}^2} + \sum_i C_i \frac{\nu_{in}\Omega_i}{{\nu_{in}}^2 + {\Omega_i}^2}\right]$$

$$\sigma_H(h) = \frac{eN_e(h)}{B(h)}\left[\frac{{\Omega_e}^2}{{\nu_{en}}^2 + {\Omega_e}^2} - \sum_i C_i \frac{{\Omega_i}^2}{{\nu_{in}}^2 + {\Omega_i}^2}\right]$$

where Ω_i is the gyro frequency, C_i is the number abundance of various ions with subscript i representing the ion species. ν_{en} (ν_{in}) is the collision frequency between electrons (ions) and neutrals, which we calculated from collision coefficients (taken from Schunk and Nagy (2009)), and neutral densities (taken from MSIS (Picone et al., 2002)). Our approach of the conductance estimate is the same as Wang and Zou (2022). Corresponding to the sudden enhancement of N_e, the Pedersen conductance transiently increased from ∼13 S to above 30 S, and the Hall conductance from a similar level to ∼25 S.

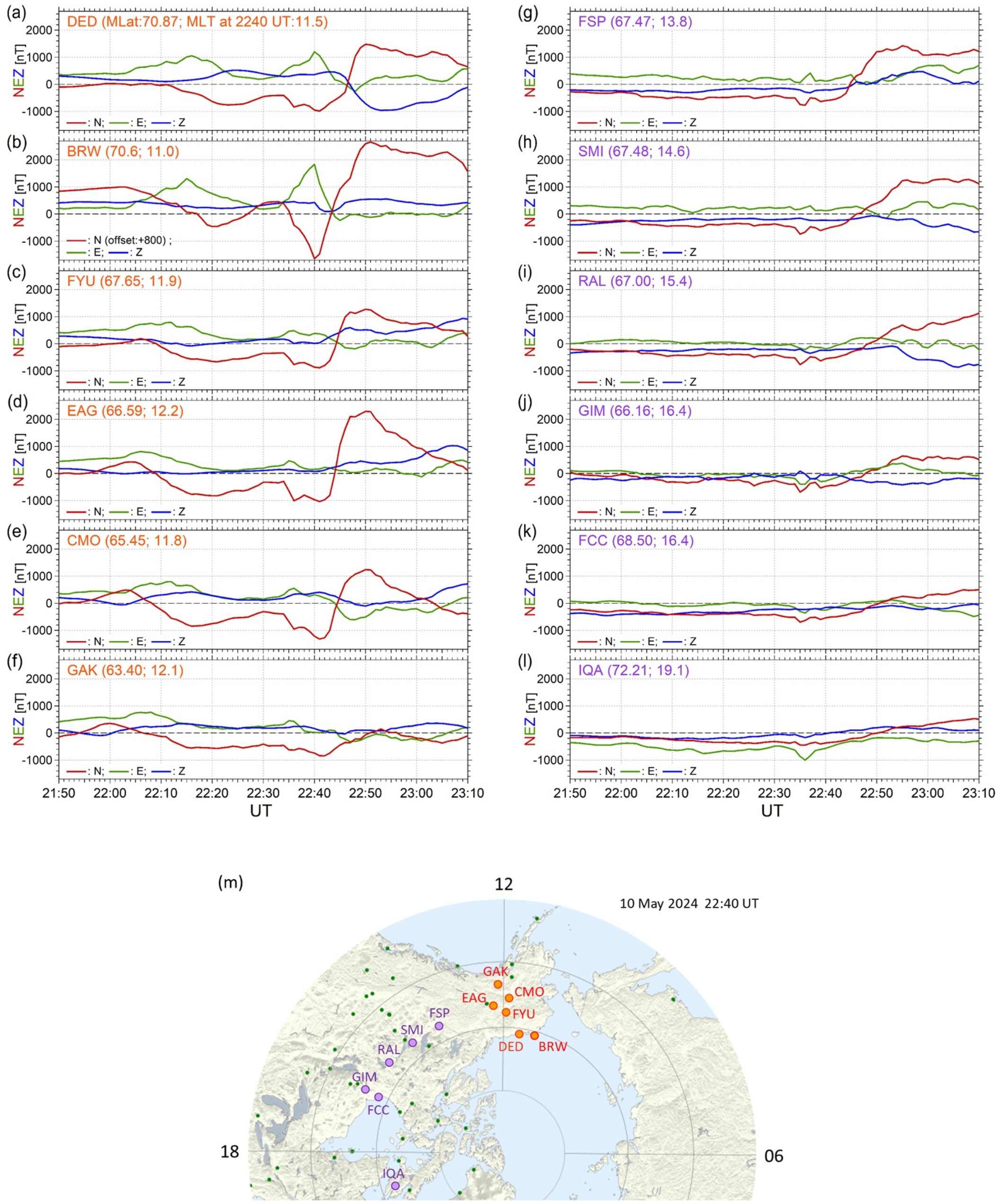

Figure 7. N (red), E (green), and Z (blue) magnetic components observed at (a) Deadhorse (DED), (b) Barrow (BRW), (c) Fort Yukon (FYU), (d) Eagle (EAG), (e) College (CMO), (f) Gakona (GAK), (g) Fort Simpson (FSP), (h) Fort Smith (SMI), (i) Rabbit Lake (RAL), (j) Gillam (GIM), (k) Fort Churchill (FCC), and (l) Iqaluit (IQA) for the interval of 2150–2310 UT on 10 May 2024. (m) The polar map of these ground stations at 2240 UT (modified from the SuperMAG polar map).

The northward electric field, E_N, increased simultaneously with N_e (Figure 9c). E_N is the electric field deduced from the measurements of beams 1, 3, and 4 in Figure 9f; each beam extends farther poleward (as shown in gray), but we used measurements closer to the radar, from 0.8 to 1.3° poleward, for the consistency of measured doppler shifts. E_N reached above 100 mV/m, which corresponds to a westward electric drift speed of ~2,000 km/s; note that "westward" is the direction of the zonal convection expected for positive IMF B_Y. Using the estimated Hall conductance, we calculated the Hall current intensity, from which we estimated the ground N disturbance assuming an infinitely-extending uniform current sheet. The result (Figure 9d) shows that not only the peak but also the overall sequence matches with the actual observation (Figure 9e). Note that the conductance enhancement

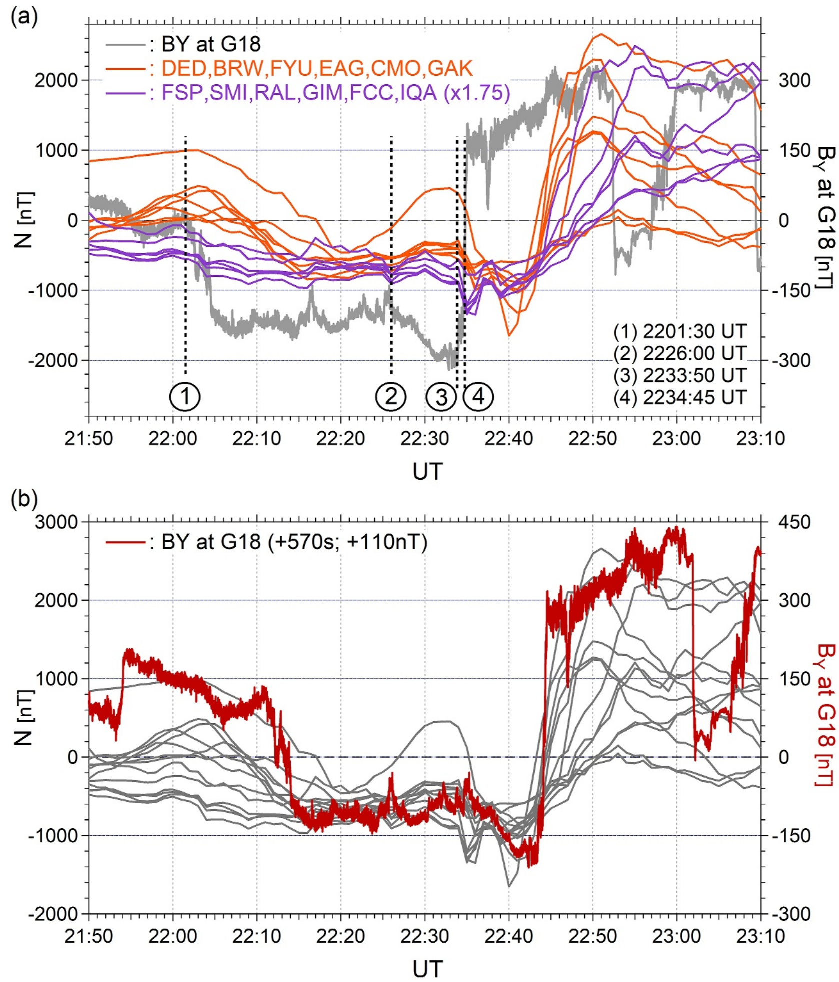

Figure 8. (a) N disturbances observed at the six stations shown in Figures 7a–7f (orange) and other six stations shown in Figures 7g–7l (purple) along with the G18 B_Y component (gray) for the interval of 2150–2310 UT on 10 May 2024. (b) The same as panel a but the N disturbances at all 12 stations in gray and the G18 B_Y component (red) shifted by +570 s (9.5 min) in time and by +110 nT vertically.

due to the precipitation enhancement made a significant contribution to this positive N disturbance. The preceding N reduction was noticeably smaller in magnitude, which may suggest that the corresponding westward AEJ developed outside, probably equatorward (because IMF B_Z was negative), of the PFISR beam coverage.

Since similar N peaks were observed in the wide ranges of MLat and MLT around PKR (Figure 8a), the E_N peak presumably reflected the temporal enhancement of the regional electric field, rather than the passing of a spatially-confined enhancement across the PFISR field of view. It is therefore suggested that this E_N enhancement marked the start of the positive B_Y-related convection. This interpretation is consistent with the simultaneous enhancement of precipitation (Figure 9a), which suggests a temporal magnetospheric process, that is, the initiation of the positive B_Y-related reconnection. Thus, the PFISR observation supports our earlier conclusion (Section 2.3) that there was a ∼10 min time delay between the G18 B_Y flip and its effect on the dayside AEJ.

3. Modeling

In this section, we compare the results of our data analysis (Section 2) with those of a global simulation. Pham et al. (2024) performed a simulation for the entire sequence of the May 2024 storm with the Multiscale Atmosphere-Geospace Environment (MAGE) model; the MAGE version that they used includes the global MHD model, GAMERA (Sorathia et al., 2020; Zhang et al., 2019), the inner magnetosphere model, RCM (Toffoletto et al., 2003), the ionospheric potential solver, REMIX (Merkin and Lyon, 2010), and the thermosphere-

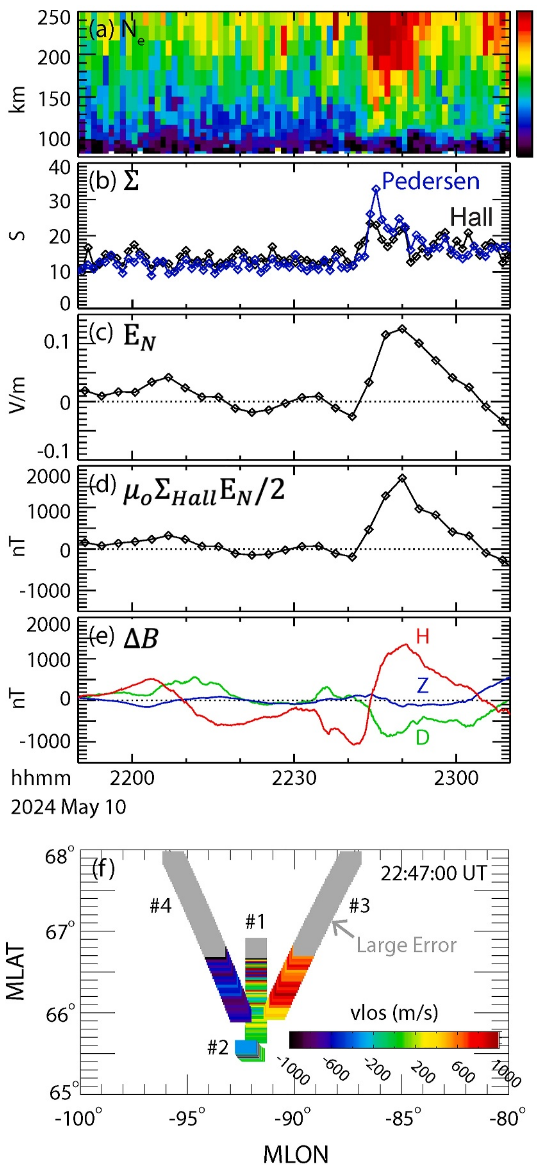

Figure 9. (a) Altitudinal profile of the electron density, N_e, (b) estimates of the Pedersen (blue) and Hall (black) conductances, (c) latitude-averaged northward electric field, E_N, (d) northward magnetic disturbance estimated from the derived Hall current intensity, (e) actual ground magnetic disturbances (H (northward): red; D (eastward): green; Z (downward): blue) at Pokar Flat (PKR), and (f) the line-of-sight velocity (positive toward the radar) measured along four beams in MLat versus MLon.

ionosphere coupling model, TIE-GCM (Richmond et al., 1992). They reconstructed a solar wind and IMF sequence from measurements made by ThC and MMS1 as well as Wind, and used it as an input for their simulation run. See Pham et al. (2024) for more details of the simulation setting.

In Figure 10a, we compare the observed (red) and reproduced (blue) sequences of the G18 B_Y component. For the model output, we sampled B_Y at $X = 6.9\ R_E$ on the X axis (of the SM coordinate system) so that the virtual satellite stays in the magnetosheath during the same interval as G18. The agreement of the two sequences is excellent for both timing and magnitude until the reentry to the magnetosphere at 2251 UT. The modeled B_Y is ~1 min ahead in time for some changes including the start of the B_Y flip, which may be attributed to the X distance of the model output slightly (~0.3 R_E) outside of geosynchronous orbit; 0.3 R_E is a ~20s travel distance at 100 km/s. Nevertheless, the excellent agreement with the G18 observation indicates that the model well reproduced the compression of the IMF and solar wind through the bow shock crossing.

Figure 11 shows the dayside polar distributions of FAC density (in color; blue and red for downward and upward FACs, respectively) and equi-potential contours every 2 min from 2231 to 2245 UT. The first two maps at 2231 and 2233 UT (Figures 11a and 11b) represent snap shots around the G18 B_Y minimum before its flip. The prenoon-side downward FAC (i.e., R1 current) is the most noticeable feature, which along with the upward FAC (i.e., R2 current) on its equatorward side, is a manifestation of an eastward convection flow in the prenoon sector. A pair of postnoon-side R1 and R2 currents coexists, but it is dominated by the prenoon-side pair as expected for the negative sign of IMF B_Y. This structure enhances further at 2235 and 2237 UT (Figures 11c and 11d) immediately after the G18 B_Y flip. At the next time step (2239 UT; Figure 11e), the prenoon-side R2 current is weaker, and the area of the prenoon-side R1 current is somewhat smaller, which presumably reflects the reduction of the negative B_Y at G18. Then, at 2241 UT (Figure 11f), an upward FAC emerges on the poleward side of the prenoon R1 current, which is the first clear sign of the positive B_Y. At the next two steps (Figures 11g and 11h), this upward FAC intensifies, and expands to the postnoon sector along with the prenoon-side downward current, which corresponds to the formation of a westward zonal flow channel and an eastward AEJ as expected for the positive turning of IMF B_Y. Thus, the overall evolution of the dayside M-I system represents what is generally expected for the negative-to-positive flip of IMF B_Y.

Now we examine more closely the timing of the transition of the modeled M-I system from its negative B_Y-driven to positive-B_Y driven state. The comparison between Figures 11e and 11f suggests that this transition takes place around 2240 UT in the model. This timing can also be confirmed with the sequence of the reproduced ground N disturbance. In Figure 10b, we compare the sequences of the reproduced (blue) and observed (red) N component at BRW. The observed disturbances are multiplied by 0.4 for comparison; the reproduced AEJ is significantly weaker than the actual one (Merkin et al., 2024), which is the subject of a future study.

Whereas the model reproduces the overall morphology of the dayside M-I system response to the G18 B_Y flip, the time difference of the ground N flip is most notable. The modeled N component starts to increase from its bottom at 2235–2236 UT, instead of 2241 UT as observed. In other words, the modeled ionosphere starts to respond to the G18 B_Y flip within 2~3 min. The time delay is at least 5 min shorter than the actual delay, which was 7–8 min for the start of the B_Y flip (i.e., the negative B_Y peak), and 9–10 min for the zero crossing of B_Y. This comparison strongly suggests that there is a process or feature that receives limited attention in modeling efforts, as well as in

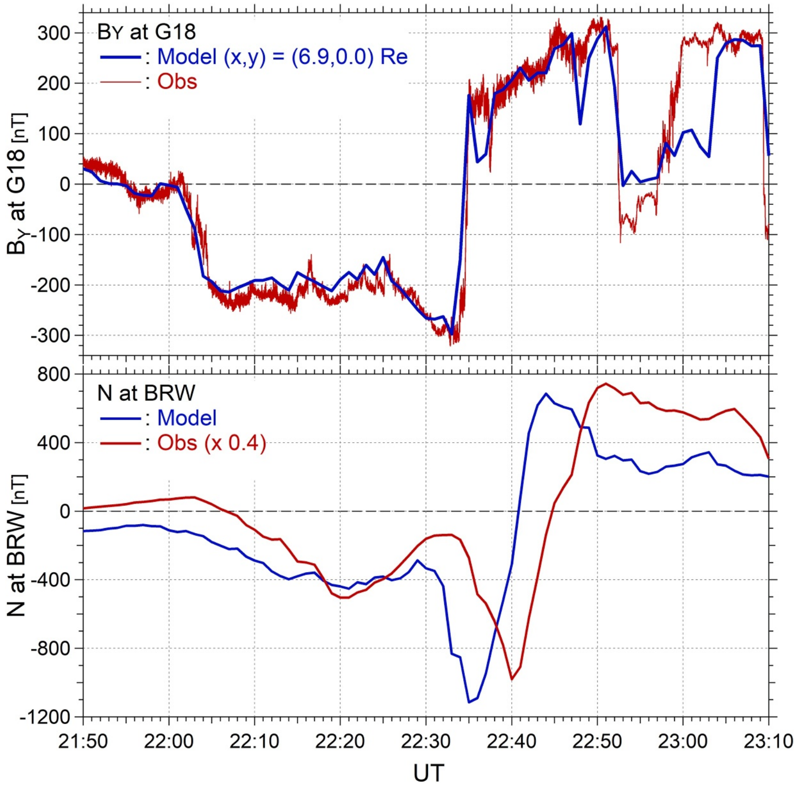

Figure 10. (a) The G18 B_Y component (red) and modeled B_Y component at $X = 6.9\ R_E$ on the Sun–Earth line (blue). (b) The observed (red) and modeled (blue) N component at Barrow (BRW). The observed N component is multiplied by 0.4.

data analyses, due to its usual insignificance, but which played a crucial role in the solar wind-magnetosphere coupling for the IMF B_Y flip of the present event.

4. Discussion

In the previous sections we examined the response of the ground magnetic field to the IMF B_Y variations during the May 2024 superstorm with an emphasis on its large and abrupt flip. We used, as a reference, the B_Y measurement made by G18 in the dayside magnetosheath. Responding to the temporal enhancement of the solar wind dynamic pressure around the B_Y flip, the midlatitude N component increased almost simultaneously (<1 min) on the dayside (Figures 4d and 5a). This is reasonable because the propagation speed of the fast magnetosonic mode

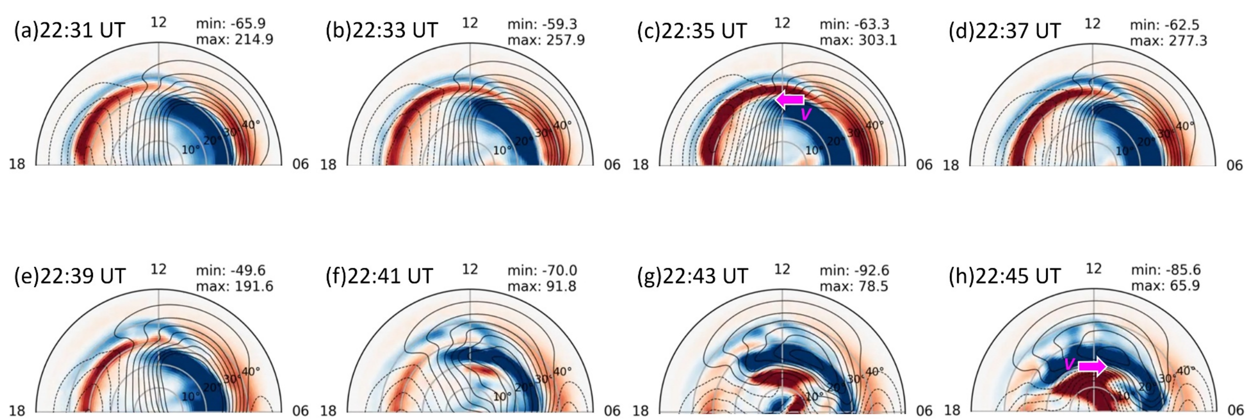

Figure 11. The dayside polar distributions of field-aligned current (FAC) density (in color; blue and red for downward and upward FACs, respectively) and equipotential contours every 2 min from 2231 to 2245 UT. The numbers in the top right of each panel are the minimum and maximum values of the potential.

10.1029/2024JA033691

(a)

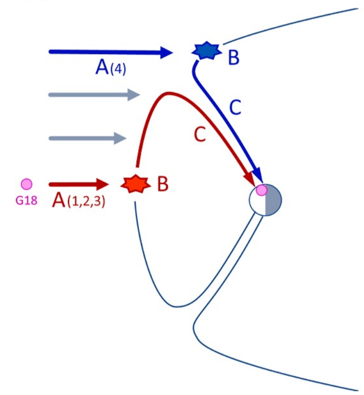

(b)

	1. B_Y (< 0) ↓ (2201:30 UT)	2. B_Y (< 0) ↓ (2226:00 UT)	3. B_Y (< 0) ↑ (2233:50 UT)	4. B_Y (= 0) ↑ (2234:44 UT)
A	→ Dayside MP	→ Dayside MP	→ Dayside MP	→ High-lat. MP
B	✓	(✓)		✓
C	✓	✓	✓	✓
Time Delay	**2~3 min**	**8 min**	**7~8 min**	**9~10 min**

Figure 12. (a) A schematic illustration of the three steps (Steps A, B, and C) of the time delay from G18 to the dayside auroral zone. (b) The tabular summary of the contribution of the three steps to the time delay from G18 to the dayside auroral zone for the four major changes of the G18 B_Y component.

easily exceeds 1,000 km/s, or 10 R_E/min, and therefore, its propagation through the dayside magnetosphere is basically instantaneous. In contrast, it took significantly longer for the effect of the G18 IMF B_Y flip to be detected in the dayside auroral zone. Although this time delay is negligible to the duration of the storm main phase, its physical implication is crucial for understanding the stormtime solar wind-magnetosphere coupling as we will discuss in the rest of this section.

Now we discuss the cause of this prolonged delay. The electric field, which is essential for driving the AEJ, is transported from the solar wind (magnetosheath) through the merging between interplanetary and terrestrial magnetic field lines. Now, as schematically shown in Figure 12a, the propagation of the electric field from G18 to the midday auroral zone consists of three steps, that is, (a) the transport of the interplanetary field lines from G18 to the reconnection site, (b) the initiation of reconnection, if required, and (c) the propagation of the electric field from the reconnection site to the auroral zone. Step A does not mean in any sense that G18 and the reconnection site were on the same stream line of the magnetosheath flow, but for this step we assume that on a magnetosheath stream line that reached the reconnection site, there was a point, around the same X distance as G18, where B_Y varied in the same way as observed by G18; this assumption can be justified by the extension of the original IMF structure over the scale of the magnetosphere (Figures 3 and 4).

Figure 12b summarizes, in a tabular form, these three steps for the four major changes of the G18 B_Y component we addressed in Section 2.3, that is, (a) the sharp reduction of G18 B_Y at 2201:30 UT, (b) the additional reduction of G18 B_Y starting at 2226:00 UT, (c) the start of the G18 B_Y flip at 2233:50 UT, and (d) the zero-crossing of G18 B_Y in the middle of its flip at 2234:45 UT; see Figure 8a. Now we discuss, for each G18 B_Y change, the contribution of the three steps to the travel time from G18 to the ground.

For step A, we need to consider two factors. The first factor is the travel distance. B_Z was negative before the B_Y flip, and therefore, for (a)–(c), the relevant reconnection site was on the dayside magnetopause, which moved to behind the dayside cusp for (d) as B_Z turned northward through the B_Y flip. Therefore, the travel distance was longer for (d), which may have contributed to the longest time delay for (d). However, the travel distance does not explain the variability of the time delays for (a)–(c).

The second factor is the speed of the magnetosheath flow. One important clue here is that the global simulation successfully reproduced the G18 B_Y sequence (Figure 10a), which suggests that the solar wind was compressed though the bow shock as we expect. In contrast, the final velocity, the velocity at which the magnetosheath plasma reaches the reconnection site, is largely unknown. However, the travel time through the magnetosheath sensitively depends on it (Samsonov et al., 2018). This final velocity may be considered as the flow speed of the inflow region of the reconnection, and therefore, closely related to the reconnection rate. Therefore, the variability of the travel times from G18 to the ground (Figure 12b) as well as the discrepancy between the model and observation may be explained in terms of the reconnection rate.

This idea is appealing because the solar wind plasma density increased significantly around the IMF B_Y flip (Figure 4d). The reconnection rate depends on the mass density and magnetic field strength on both sides of the current sheet as well as the aspect ratio of the effective diffusion region (e.g., Cassak and Shay, 2007). The reconnection rate decreases inversely proportional to the square root of the effective mass density, which is given by $(\rho_1 B_2 + \rho_2 B_1)/(\rho_1 + \rho_2)$ with the mass density ρ_i and the total magnetic field B_i on the different sides ($i = 1$ and 2) of the current sheet; see Eq. 17 of Cassak and Shay (2007). Therefore, if the solar wind mass density increases significantly as observed in this event (Figure 4d), the reconnection rate decreases, and so does the inflow velocity. This idea explains, at least qualitatively, why the time delay was significantly shorter for (a), and became longer for (b) and (c). For the high-latitude reconnection of (d), open field lines that had reconnected with preceding negative B_Y interplanetary field lines (the magenta field line in Figure 1a) needed to be removed, which may have made an additional contribution to the deceleration of the magnetosheath flow.

We note, however, that in the present event, the relationship between the delay time and the plasma density was not simple. If we propagate the MMS1 and THEMIS measurements of N_{SW} to the G18 location based on the time lags of the B_Y flip (not shown), N_{SW} would be 10–15 cm^{-3} for (a), 30–40 cm^{-3} for (b), and $\sim$100 cm^{-3} for (c) and (d); the actual density was probably four times larger if compressed through the bow shock crossing by the same ratio as the magnetic field through the bow shock crossing. In contrast, the G18-to-ground time delay jumped between (a) and (b), but did not change significantly afterward (Figure 12b). However, this result does not necessarily contradict our interpretation because what is crucial for the reconnection rate is the plasma density in the inflow region, and the magnetosheath plasma density does not necessarily represent the effective density of the dayside reconnection even though they are probably loosely correlated. Let us consider an extreme case in which the reconnection is already so slow, due to a highly dense magnetosheath plasma, that field lines are piling up in the subsolar magnetosheath. In such a case, magnetosheath flows are mostly deflected before reaching the magnetopause, and accordingly, the plasma density in the inflow region would be determined by a flow pattern in the vicinity of the reconnection site, which could level off even if the solar wind density increases further. If such a situation was realized by the time of (b), it is possible that the delay time remained similar for (c) and (d).

Step B, the response time of the reconnection, is an important issue, but is unlikely the cause of the wide variability of the time delays. The initiation of reconnection is expected for (a) and (d), and possibly also for (b) if the reconnection site moved as the magnitude of negative B_Y increased. For (c), it is expected that the dayside reconnection rate decreased sharply as the B_Y flip started. Although the aforementioned enhancement of the solar wind number density may have delayed the onset of reconnection for (b) and (d), the associated timescale is on a kinetic scale; Wu et al. (2011) reported that it is 10s of the ion gyroperiod, which was of the order of 1s in the present case. Apparently, the observed time delays were not organized or influenced by step B.

Step C, the propagation from the reconnection site to the dayside auroral zone is required for each of (a)–(d). The associated delay is the Alfvén travel time from the magnetopause to the ionosphere. For (d), the Alfvén travel time is uncertain as we do not know how far behind the cusp the reconnection site was located. For the dayside magnetopause reconnection, (a)–(c), the Alfvén travel time is usually 1 minute or less; it should be about a quarter of the fundamental eigenperiod of standing oscillations as observed as Pc4–5 pulsations. Since the magnetopause was inside geosynchronous orbit, it is improbable that the propagation distance changed significantly in this event. Therefore, for step C to be the primary cause of the observed difference in time delay, the Alfvén velocity would have to decrease by a factor of $\sim$3, which requires an enhancement of the mass density by an order of magnitude. However, we cannot find any change of internal conditions that might have enhanced the mass density by such a magnitude during this event (Figure 2). In fact, the effect of the dynamic pressure enhancement propagated instantaneously from G18 to the ground. The enhancement of the solar wind plasma density might have increased the plasma density in the magnetosphere, for example, through the dayside reconnection, but its effect on the Alfvén travel time is unclear. Thus, although we cannot entirely dismiss the possibility that step C contributed to the variability in time delay, it is highly questionable that this step played a decisive role.

Thus, based on our consideration of Steps A, B, and C, we suggest that the solar wind density enhancement was the primary cause of the variability of the G18-to-ground time delays, for which the reconnection rate at the dayside magnetopause is crucial. However, as we addressed earlier, the dependence of the reconnection rate on the solar wind density is not straightforward. Although in general, modeling is a promising approach for such a complex issue, for this event, the MAGE model reproduces the BRW magnetic disturbance with a much shorter time delay (Figure 10b), suggesting that the model overestimates the dayside reconnection rate. Thus, the solar

Journal of Geophysical Research: Space Physics 10.1029/2024JA033691

wind-magnetosphere interaction under extremely dense solar wind conditions, as we addressed in the present study, also presents a critical new challenge for modeling superstorms.

In closing, we would like to make two points. First, the stormtime mass loading and the associated reduction of the dayside reconnection rate has been addressed in terms of the formation of plasmaspheric plumes (Borovsky and Denton, 2006; Walsh et al., 2013, 2014) and warm plasma cloaks (Fuselier et al., 2017). The number density of these structures is typically in the range of 10–100 cm^{-3}; see Goldstein et al. (2004) and the references cited above. Whereas the associated density enhancement may reduce the reconnection rate as much as 20% (Fuselier et al., 2017), its global effect still remains to be understood (Zhang et al., 2016). In the present event, in contrast, the peak number density exceeded 100 cm^{-3} in the solar wind (Figure 4d), and probably increased to ∼400 cm^{-3} through the bow shock crossing. Moreover, the associated structure extended over the entire dayside magnetosphere (Section 2.1). It is therefore highly conceivable that the extreme solar wind density enhancement as observed in this event makes a far more significant impact on the energy coupling between the solar wind and the magnetosphere.

Second, we would like to reemphasize that the magnitude of the response was extraordinary. Responding to the B_Y flip, the ground N component increased by a few thousands of nT, by 4,300 nT at BRW, in ∼10 min in the prenoon auroral zone. The IMF B_Z component is generally considered as a measure of the external driving of geomagnetic disturbances, for which we consider nightside substorm activity or dawnside AEJ intensification as a manifestation of global convection enhancement (Ohtani, 2021; Ohtani et al., 2023). In the present event, however, it was the IMF B_Y component that played a crucial role in this extraordinary event, and the ground magnetic field changed most significantly and sharply in the midday sector. Apparently, the dayside AEJ can be a cause of potentially hazardous geomagnetic disturbances, even though it is not widely recognized, and the magnetopause reconnection is its direct driver. Thus, the reconnection rate as discussed in this section is crucial not only for better understanding the stormtime solar wind-magnetosphere coupling but also for assessing the risk of stormtime geomagnetic hazards.

5. Summary

In the present study we used the G18 magnetic field measurements as a reference, and examined how the dayside ground magnetic field responded to the B_Y variations, especially to its extraordinarily large and abrupt flip, during the May 2024 geomagnetic storm. The ground N component changed by thousands of nT from strongly negative to strongly positive, and the overall response was consistent with the idea that the direction of the primary AEJ changed from westward to eastward responding to the negative-to-positive IMF B_Y flip. We paid special attention to the time delay from G18 to the ground, which changed significantly during the course of the event. For the initial G18 B_Y reduction, which took place ∼30 min prior to the B_Y flip, the time delay was 2–3 min. The time delay was significantly longer for the later B_Y changes; for example, it was 7–8 min for the start of the B_Y flip, and 9–10 min for the subsequent zero crossing of B_Y. We discussed these time delays in terms of three steps of the propagation from G18 to the ground, that is, (a) the transport of magnetic field lines from G18 to the reconnection site, (b) the initiation of the reconnection, (c) Alfvén wave propagation from the reconnection site to the dayside ionosphere. It is highly questionable that steps B and C played any decisive role in the G18-to-ground propagation. In contrast, step A possibly explains the variability of the time delays. Around the time of the B_Y flip, the solar wind number density increased to above 100 cm^{-3}, and additionally by a factor of ∼4 through the bow shock crossing. This density enhancement presumably reduced the reconnection rate at the dayside magnetopause, and therefore, increased the travel time from G18 to the reconnection site (by slowing down the inflow). We also found that the MAGE global simulation reproduces the westward-to-eastward flip of the midday AEJ but with a time delay significantly shorter than the actual delay (by ∼5 min). The discrepancy may imply that the model overestimates the dayside reconnection rate. Whereas the effect of the mass loading on the solar wind—magnetosphere coupling is often addressed in terms of internal processes, the present study suggests that solar wind structures can make a significant impact under extreme conditions.

Data Availability Statement

SuperMAG indices, polar maps of ground magnetic disturbances, and magnetic field data at individual stations are available at the SuperMAG site (https://supermag.jhuapl.edu/). The OMNI data are available at the NASA

OMNI website (https://omniweb.gsfc.nasa.gov/). The MMS data are available at https://lasp.colorado.edu/mms/sdc/public/, and the THEMIS data are available at http://themis.ssl.berkeley.edu/data/themis/. The GOES-18 data are available at the NOAA GOES-R Space Weather site (https://www.ngdc.noaa.gov/stp/satellite/goes-r.html). The PHISR data are available at the SRI AMISR website (https://amisr.com/amisr/links/data-access/).

Acknowledgments

We are most grateful to the members of the Center for Geospace Storms (CGS) team (https://cgs.jhuapl.edu/) for fruitful discussions. We are also very grateful to the NSF SuperMAG facility, the NOAA National Centers for Environmental Information, the SRI PHISR project, the NASA MMS and THEMIS missions for providing data for this study. This work was supported by the NASA DRIVE Science CGS under award 80NSSC22M0163, and by the NSF National Center for Atmospheric Research (NCAR), which is a major facility sponsored by under Cooperative Agreement No. 1852977. We would also like to acknowledge high-performance computing support from the Derecho system (https://doi.org/10.5065/qx9a-pg09) provided by the NSF NCAR. Work at APL was also supported by NSF Grants 2224986 (SO), 2403939 (JWG), NASA Grants 80NSSC21K0036 (SO), 80NSSC24K1113 (JWG, SO). SR acknowledges additional support by the JHU/APL Independent R&D fund, and by the NASA MMS mission via subcontract to the Southwest Research Institute (NNG04EB99C). SuperMAG indices and polar maps used in this study were derived from ground magnetometer data provided by many organizations and institutes as listed at https://supermag.jhuapl.edu/info/?page=acknowledgement. We also gratefully acknowledge that magnetometer data used in this study were provided, through SuperMAG, by the following projects and agencies: Geophysical Institute Magnetometer Array (PI: Don Hampton; https://www.gi.alaska.edu/monitors/magnetometer/about; GIMA) for data from Barrow, College, Eagle, Fort Yukon, Gakona, Poker Flat; Canadian Array for Realtime Investigations of Magnetic Activity (https://www.carisma.ca/; PI: Ian Mann) for data from Fort Churchill, Fort Simpson, Fort Smith, Gillam, and Rabbit Lake; U.S. Geological Survey (https://www.usgs.gov/programs/geomagnetism) for Bay St Louis, Deadhorse, Fresno, Tucson; CANadian Magnetic Observatory System (https://geomag.nrcan.gc.ca/obs/canmos-en.php; CANMOS) for data from Iqaluit.

References

Araki, T. (1994). A physical model of the geomagnetic sudden commencement. *American Geophysical Union Geophysical Monograph Series*, *81*, 183–200. https://doi.org/10.1029/GM081p0183

Borovsky, J. E., & Denton, M. H. (2006). Effect of plasmaspheric drainage plumes on solar-wind/magnetosphere coupling. *Geophysical Research Letters*, *33*(20), L20101. https://doi.org/10.1029/2006GL026519

Burch, J. L., Reiff, P. H., Menietti, J. D., Heelis, R. A., Hanson, W. B., Shawhan, S. D., et al. (1985). IMF B_y -dependent plasma flow and Birkeland currents in the dayside magnetosphere: 1. Dynamics explorer observations. *Journal of Geophysical Research*, *90*(A2), 1577–1593. https://doi.org/10.1029/JA090iA02p01577

Cassak, P. A., & Shay, M. A. (2007). Scaling of asymmetric magnetic reconnection: General theory and collisional simulations. *Physics of Plasmas*, *14*(10), 102–114. https://doi.org/10.1063/1.2795630

Cliver, E. W., & Svalgaard, L. (2004). The 1989 solar terrestrial disturbances and current limits of extreme space weather activity. *Solar Physics*, *224*(1–2), 407–422. https://doi.org/10.1007/s11207-005-4980-z

Cowley, S., & Lockwood, M. (1992). Excitation and decay of solar wind-driven flows in the magnetosphere-ionosphere system. *Annales Geophysicae*, *10*, 103–115.

Edwards, T. R., Weimer, D. R., Olsen, N., Lühr, H., Tobiska, W. K., & Anderson, B. J. (2020). A third generation field-aligned current model. *Journal of Geophysical Research: Space Physics*, *125*(1), e2019JA027249. https://doi.org/10.1029/2019JA027249

Friis-Christensen, E., & Wilhjelm, J. (1975). Polar cap currents for different directions of the interplanetary magnetic field in the *Y-Z* plane. *Journal of Geophysical Research*, *80*(10), 1248–1260. https://doi.org/10.1029/JA080i010p01248

Fuselier, S. A., Burch, J. L., Mukherjee, J., Genestreti, K. J., Vines, S. K., Gomez, R., et al. (2017). Magnetospheric ion influence at the dayside magnetopause. *Journal of Geophysical Research: Space Physics*, *122*(8), 8617–8631. https://doi.org/10.1002/2017JA024515

Gjerloev, J. W. (2012). The SuperMAG data processing technique. *Journal of Geophysical Research*, *117*(A9), A09213. https://doi.org/10.1029/2012JA017683

Goldstein, J., Sandel, B. R., Thomsen, M. F., Spasojević, M., & Reiff, P. H. (2004). Simultaneous remote sensing and in situ observations of plasmaspheric drainage plumes. *Journal of Geophysical Research*, *109*(A3), A03202. https://doi.org/10.1029/2003JA010281

Heelis, R. A. (1984). The effects of interplanetary magnetic field orientation on dayside high-latitude ionospheric convection. *Journal of Geophysical Research*, *89*(A5), 2873–2880. https://doi.org/10.1029/JA089iA05p02873

Heppner, J. P., & Maynard, N. C. (1987). Empirical high-latitude electric field models. *Journal of Geophysical Research*, *92*(A5), 4467–4489. https://doi.org/10.1029/JA092iA05p04467

Iijima, T., Fujii, R., Potemra, T. A., & Saflekos, N. A. (1978). Field-aligned currents in the south polar cusp and their relationship to the interplanetary magnetic field. *Journal of Geophysical Research*, *83*(A12), 5595–5603. https://doi.org/10.1029/JA083iA12p05595

Love, J. J. (2021). Extreme-event magnetic storm probabilities derived from rank statistics of historical Dst intensities for solar cycles 14–24. *Space Weather*, *19*(4), e2020SW002579. https://doi.org/10.1029/2020SW002579

Merkin, V. G., & Lyon, J. G. (2010). Effects of the low-latitude ionospheric boundary condition on the global magnetosphere. *Journal of Geophysical Research*, *115*(A10), A10202. https://doi.org/10.1029/2010JA015461

Merkin, V. G., Wanner, T., Ohtani, S., Zou, Y., Pham, K. H., & Sorathia, K. (2024). A story of two IMF by flips during the May 2024 "Gannon" superstorm. In *Abstract (SM31C-2567) presented at AGU24, 9-13 Dec 2024*. Retrieved from https://agu.confex.com/agu/agu24/meetingapp.cgi/Paper/1673702

Murr, D. L., & Hughes, W. J. (2001). Reconfiguration timescales of ionospheric convection. *Geophysical Research Letters*, *28*(11), 2145–2148. https://doi.org/10.1029/2000GL012765

Newell, P. T., & Gjerloev, J. W. (2011). Evaluation of SuperMAG auroral electrojet indices as indicators of substorms and auroral power. *Journal of Geophysical Research*, *116*(A12), A12211. https://doi.org/10.1029/2011JA016779

Newell, P. T., & Gjerloev, J. W. (2012). SuperMAG-based partial ring current indices. *Journal of Geophysical Research: Space Physics*, *117*(A5), A05215. https://doi.org/10.1029/2012JA017586

Ohtani, S. (2021). Revisiting the partial ring current model: Longitudinal asymmetry of ground magnetic depression during geomagnetic storms. *Journal of Geophysical Research: Space Physics*, *126*(9), e2021JA029643. https://doi.org/10.1029/2021JA029643

Ohtani, S., Sorathia, K., Merkin, V. G., Frey, H. U., & Gjerloev, J. W. (2023). External and internal causes of the stormtime intensification of the dawnside westward auroral electrojet. *Journal of Geophysical Research: Space Physics*, *128*, e2023JA031457. https://doi.org/10.1029/e2023JA031457

Pham, K., Wu, H., Wang, W., Hairston, M. R., Lin, D., & Merkin, V. (2024). Significant ionospheric response during the May 2024 storm, abstract (SA31B-04) presented at AGU24, 9-13 Dec 2024. Retrieved from https://agu.confex.com/agu/agu24/meetingapp.cgi/Paper/1733743

Picone, J. M., Hedin, A. E., Drob, D. P., & Aikin, A. C. (2002). NRLMSISE-00 empirical model of the atmosphere: Statistical comparisons and scientific issues. *Journal of Geophysical Research*, *107*(A12), SIA15-1–SIA15-16. https://doi.org/10.1029/2002ja009430

Richmond, A. D., Ridley, E. C., & Roble, R. G. (1992). A thermosphere/ionosphere general circulation model with coupled electrodynamics. *Geophysical Research Letters*, *6*, 601–604. https://doi.org/10.1029/92gl00401

Ridley, A. J., Lu, G., Clauer, C. R., & Papitashvili, V. O. (1998). A statistical study of the ionospheric convection response to changing interplanetary magnetic field conditions using the assimilative mapping of ionospheric electrodynamics technique. *Journal of Geophysical Research*, *103*(A3), 4023–4039. https://doi.org/10.1029/97JA03328

Ruohoniemi, J. M., & Greenwald, R. A. (1998). The response of high-latitude convection to a sudden southward IMF turning. *Geophysical Research Letters*, *25*(15), 2913–2916. https://doi.org/10.1029/98GL02212

Samsonov, A. A., Sibeck, D. G., Dmitrieva, N. P., Semenov, V. S., Slivka, K. Y., Šafránkova, J., & Němeček, Z. (2018). Magnetosheath propagation time of solar wind directional discontinuities. *Journal of Geophysical Research: Space Physics*, *123*(5), 3727–3741. https://doi.org/10.1029/2017JA025174

Schunk, R., & Nagy, A. (2009). *Ionospheres: Physics, plasma physics, and chemistry*. Cambridge University Press.

Sorathia, K. A., Merkin, V. G., Panov, E. V., Zhang, B., Lyon, J. G., Garretson, J., et al. (2020). Ballooning-interchange instability in the near-Earth plasma sheet and auroral beads: Global magnetospheric modeling at the limit of the MHD approximation. *Geophysical Research Letters*, *47*(14), e2020GL088227. https://doi.org/10.1029/2020GL088227

Toffoletto, F., Sazykin, S., Spiro, R., & Wolf, R. (2003). Inner magnetospheric modeling with the rice convection model. *Space Science Reviews*, *107*(1–2), 175–196. https://doi.org/10.1023/a:1025532008047

Walsh, B. M., Foster, J. C., Erickson, P. J., & Sibeck, D. G. (2014). Simultaneous ground and space-Based observations of the plasmaspheric Plume and magnetospheric reconnection. *Science*, *343*(6175), 1122–1125. https://doi.org/10.1126/science.1247212

Walsh, B. M., Sibeck, D. G., Nishimura, Y., & Angelopoulos, V. (2013). Statistical analysis of the plasmaspheric plume at the magnetopause. *Journal of Geophysical Research: Space Physics*, *118*(8), 4844–4851. https://doi.org/10.1002/jgra.50458

Wang, Z., & Zou, S. (2022). Compass: A new COnductance model based on PFISR and SWARM satellite observations. *Space Weather*, *20*(2), e2021SW002958. https://doi.org/10.1029/2021sw002958

Weimer, D. R. (2005). Improved ionospheric electrodynamic models and application to calculating Joule heating rates. *Journal of Geophysical Research*, *110*(A5), A05306. https://doi.org/10.1029/2004JA010884

Wilhjelm, J., Friis-Christensen, E., & Potemra, T. A. (1978). The relationship between ionospheric and field-aligned currents in the dayside cusp. *Journal of Geophysical Research*, *83*(A12), 5586–5594. https://doi.org/10.1029/JA083iA12p05586

Wu, P., Shay, M. A., Phan, T. D., Oieroset, M., & Oka, M. (2011). Effect of inflow density on ion diffusion region of magnetic reconnection: Particle-in-cell simulations. *Physics of Plasmas*, *18*(11), 111204. https://doi.org/10.1063/1.3641964

Zhang, B., Brambles, O. J., Wiltberger, M., Lotko, W., Ouellette, J. E., & Lyon, J. G. (2016). How does mass loading impact local versus global control on dayside reconnection? *Geophysical Research Letters*, *43*(5), 1837–1844. https://doi.org/10.1002/2016GL068005

Zhang, B., Sorathia, K. A., Lyon, J. G., Merkin, V. G., Garretson, J. S., & Wiltberger, M. (2019). Gamera: A three-dimensional finite-volume MHD solver for non-orthogonal curvilinear geometries. *The Astrophysical Journal - Supplement Series*, *244*(1), 20. https://doi.org/10.3847/1538-4365/ab3a4c